



Aerodynamic loads measurement and flow visualization of an ogive in a supersonic flow

Stefano Boccelli, Ruben Di Battista, Maxim Van Cappellen

December 5, 2016

Abstract

The behavior of supersonic flow around a slender body (a von Karman-shaped nose-cone) was studied in this work. The nose-cone, or ogive, was subjected to a flow at Mach 3.5 in the S-4 blow-down wind tunnel. The forces on the ogive were measured for different angles of attack by use of an internal 3-component sting balance. The calibration method and the data acquisition chain are presented and the results are commented accordingly. The resulting force and moment coefficients of the ogive were thereafter compared to analytical solutions. Good accordance is reported for both axial and lift coefficients, while the drag coefficient is underpredicted by the theoretical methods. The shockwave behavior around the ogive is studied by three visualisation techniques: shadowgraph and schlieren, oil visualisation and by use of a water-table. Both the shadowgraph and oil visualisation experiments were performed in the S-4 wind tunnel. The results were compared to theoretical shock behavior and to the hydraulic analogy provided by the water-table experiments. Merging the outcomes of the schlieren, oil visualization and water table was possible to propose an interpretation of the flow pattern while the shadowgraph was unable to provide meaningful results.

Keywords: *supersonic, ogive, flow visualization, strain gauges, balance, slender body, conical shock waves, body of revolution*

Contents			
		6.2.2 Inclined Flow	12
		6.2.3 Rear-part of the ogive	13
		6.3 Water Table	13
1 Introduction	2	6.3.1 Estimation of the water depth	14
		6.3.2 Validity of the hydraulic analogy	14
2 Theoretical Background	2	6.3.3 Qualitative Flow Pattern Analysis	14
2.1 Flow past a cone	2		
2.2 Slender body theory	2	References	16
3 Experimental Setup	3		
3.1 Wind Tunnel	3		
3.2 Schlieren and Shadowgraph	3		
3.3 Water Table	3		
4 Calibration	3		
4.1 Incidence calibration	3		
4.2 Pressure transducer calibration	3		
4.2.1 Uncertainty determination	4		
4.3 Balance calibration	4		
4.3.1 Validation of the calibration matrix	5		
5 Results	6		
5.1 Center of gravity and aerodynamic center	6		
5.2 Aerodynamic coefficients	6		
5.3 Uncertainty analysis	8		
6 Flow Visualization	10		
6.1 Oil visualization	10		
6.2 Shadowgraph and Schlieren	10		
6.2.1 Axial Flow	11		

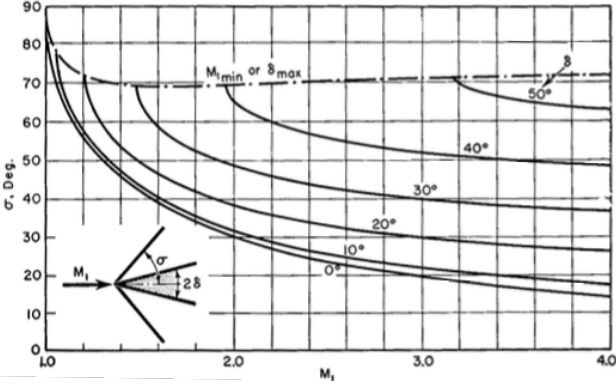


Figure 1: Solution of eq. (1)

1. Introduction

The objective of this lab is to investigate the behavior of compressible flow around a slender body (an ogive). The lab consists of two main experiments: in the first part the aerodynamic coefficients of the ogive are determined by subjecting the model to a supersonic flow at Mach 3.5. In the second part the flow around the ogive is visualised by use of shadowgraph/schlieren, oil visualisation and by use of a water table.

2. Theoretical Background

2.1. Flow past a cone

The solution of the supersonic flow over a conical body of revolution is reported in [1] to be governed by eq. (1). This equation can be solved numerically as explained in [2].

$$\frac{1}{c} \frac{d^2 u_r}{d\theta^2} \left\{ \frac{\gamma+1}{2c^2} \left(\frac{du_r}{d\theta} \right)^2 - \frac{\gamma-1}{2} \left(1 - \frac{u_r^2}{c^2} \right) \right\} =$$

$$(\gamma-1) \frac{u_r}{c} \left(1 - \frac{u_r^2}{c^2} \right) + \frac{\gamma-1}{2c} \left(1 - \frac{u_r^2}{c^2} \right) \cot \theta \frac{du_r}{d\theta} -$$

$$\frac{\gamma u_r}{c^3} \left(\frac{du_r}{d\theta} \right)^2 - \frac{\gamma-1}{2c^3} \cot \theta \left(\frac{du_r}{d\theta} \right)^3 \quad (1)$$

In fig. 1 the solution of eq. (1) is given in terms of shockwave angle on cone angle. The nosecone profile is provided by eq. (2) as a body of revolution. The semiangle of the ogive at the nose tip can be further derived computing the derivative of the thickness

distribution function (eq. (2)) and developing it in Taylor series around $x = 0$ as showed in eq. (3). A direct computation returns a nose half-angle of $\sim 13^\circ$.

$$R(x) = \frac{L}{2F} \left[1 - \left(\frac{x-L}{L} \right)^2 \right] \quad (2)$$

$$\left. \frac{dR}{dx} \right|_{x=0} = \frac{1}{F} = \frac{D}{L} \quad (3)$$

2.2. Slender body theory

A simplified approach to the study of aerodynamic forces acting on a body of revolution is provided by the so called *slender body theory*. Such theory applies to slender bodies of revolution, where the presence of the body may be introduced as a small velocity perturbation to an otherwise uniform flow. The equation to be solved is:

$$(1 - M_\infty^2) \frac{\partial^2 \phi}{\partial x^2} + \frac{\partial^2 \phi}{\partial y^2} + \frac{\partial^2 \phi}{\partial z^2} = 0 \quad (4)$$

where ϕ is the velocity perturbation. The solution may be obtained by distributing sources along the symmetry axis and imposing the tangency condition on the body wall, see [3]. The result, first obtained by von Kármán, leads to an expression for the drag coefficient:

$$S(L)C_{D1} = -\frac{1}{\pi} \int_0^L \int_0^x S''(\xi) S''(x) d\xi dx \quad (5)$$

where S is the ogive cross section, S'' its second spatial derivative and L the length of the body. eq. (5) evaluated for the given body returns a value $S(L)C_{D1} = 6.122 \times 10^{-5}$. The procedure has been generalized to yawed bodies of revolution by Tsien [4], by exploiting linearity and introducing a cross-flow. Following the derivation in [3], the normal and axial forces can be expressed and rotated, to obtain lift and drag:

$$\begin{cases} N = 2\alpha q_\infty S(L) \\ A = q_\infty S(L)C_{D1} - q_\infty S(L)\alpha^2 \end{cases} \Rightarrow \begin{cases} L = N \cos \alpha - A \sin \alpha \\ D = N \sin \alpha + A \cos \alpha \end{cases}$$

α being the angle of attack and q_∞ the dynamic pressure of the free stream.

It's important to remark that this theory is linear and typically holds significant error for the drag prediction. Moreover, its validity is limited to the range of angles of attack where flow remains attached, condition which in the present case is satisfied, according to the performed flow visualization.

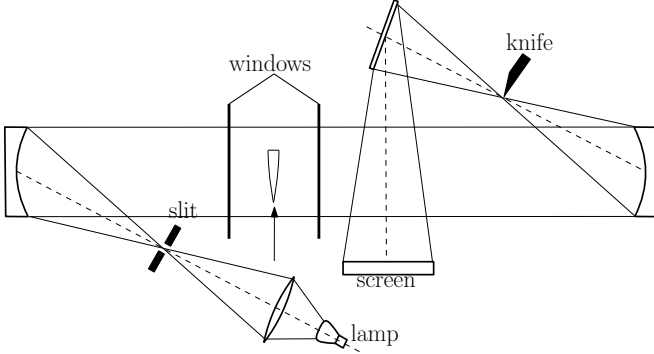


Figure 2: Sketch of the setup for the shadowgraph and schlieren

3. Experimental Setup

3.1. Wind Tunnel

The measurement of the aerodynamic loads on the ogive have been performed in the von Karman Institute (VKI)'s S4 blow-down supersonic wind tunnel, the test-area of the tunnel is 8×10 cm. A sting-type AR3820 3-axis balance, produced internally at VKI, has been used. The strain-gauges have been connected to a Wheatstone bridge conditioning system and the signal was then digitalized by a NI DAS on a DELL computer. The wind tunnel is equipped with an incidence-varying mechanism based on a stepper motor, able to change the angle of attack during the experiment by using a turns regulator.

3.2. Schlieren and Shadowgraph

For the shadowgraph and schlieren visualizations a sketch of the basic configuration is reported in fig. 2. A light source provided by a standard light bulb is focused with a slit and pointed to a mirror that directs the light ray parallelly towards the test section to another mirror that orients the light ray in the direction of a knife, placed in the focal point¹. The image is then mirrored to a screen on the other side of the room.

3.3. Water Table

The water table is composed by a 1.6m-long \times 0.9m-wide slightly inclined table topped by a reservoir whose water flow rate can be regulated. The water depth can be regulated modifying the inflow rate or also regulating the height of a knife placed just after

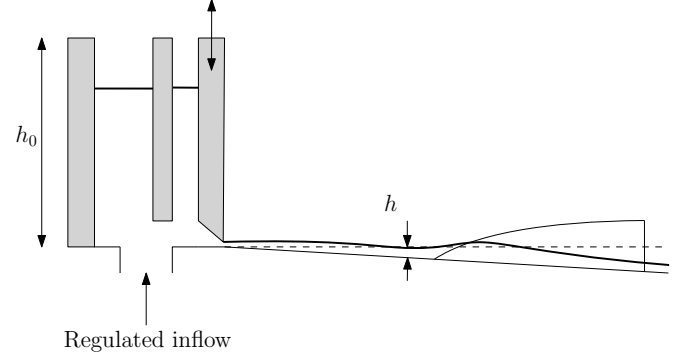


Figure 3: Sketch of the setup for the water table visualizations

the reservoir. On the bottom of the slightly inclined plane, that is transparent, a light to enhance the visibility of the flow pattern can be turned on. A simplified sketch of the setup is reported in fig. 3.

4. Calibration

4.1. Incidence calibration

The output of the incidence mechanism is given in terms of turns of the motor shaft and has to be linked to the actual model incidence. The calibration was performed connecting a flat plate to the movable sting and using skewed plexiglass blocks to generate a reference angle. The sting was then moved until a zero incidence was reached, checked using a bubble level.

The calibration curve reads:

$$N_t = -32.25 \alpha_{deg} - 1.18 \pm 7 \quad (20 : 1) \quad (6)$$

where N_t is the number of turns of the motor shaft and α_{deg} the incidence expressed in degrees. The uncertainty of ± 7 turns was found empirically, being basically the uncertainty of the bubble level, scaled to represent a 95% confidence level. In terms of angle of attack the uncertainty becomes: $\delta \alpha_{deg} \approx 0.2^\circ$.

4.2. Pressure transducer calibration

The pressure transducer used for the reservoir stagnation pressure measurement is a Valydine sensor that is a differential transducer that measures the difference between the two provided channels, one for ambient pressure, the other for the reservoir pressure. The

¹the knife is present only for the schlieren tests

variation of atmospheric pressure from the moment of calibration to the moment of performing the actual experiments was found to be around 0.2% of the reservoir pressure. This effect was thus neglected.

The calibration has been performed using an hydraulic pressure calibrator. This device consists of a vertical piston inserted into a chamber filled with oil. On top of the piston weights can be stacked to increase the pressure. The piston is raised and leveled to be free in order to have the pressure from weights acting on the oil instead of the external case. Several weights have been tested separately recording the voltage output of the pressure transducer. At the beginning problems have been experienced with anomalies in the returned voltage values: the error has been stated to be caused by static friction of the piston disk against vertical walls; the solution provided to this issue has been to put in slow rotation the disk before measuring in order to reduce this bias effect. Moreover a slow constant drift has also been recorded, probably due to a small leak, hence the calibration operations have been performed as fast as possible. The calibration law is reported in fig. 4.

4.2.1. Uncertainty determination

The uncertainty on the voltage value has been computed considering the fitting line $V = f(P)$ obtained by a least-squares approach on a set of calibration measurements performed applying a set of known loads F_i over the hydraulic calibrator, hence giving a set of applied pressure values p_i , and retrieving a set of voltages V_i as a response. The uncertainty on the value of the loads has been neglected so the only contribute is given by uncertainty on the fitting; this has been estimated as for section 5.3 where $e_i = V_i - f(p_i)$ is the fitting error and $f(p_i)$ is the linear fitting function. Assuming that the uncertainties for the coefficients of the regression line $\delta k, \delta b$ are negligible, the computed uncertainty value obtained is:

$$\delta p = 0.072 [\text{bar}]$$

4.3. Balance calibration

Before starting the calibration, the acquisition system was configured. The acquisition system has a range between $\pm 5V$ and the maximum axial load on the balance is 20N. The amplifier is regulated such that the balance output, corresponding to the 5V limit of the acquisition system. The Nyquist filter was regulated at 10kHz and the sampling frequency was set at 1kHz. By doing this the signal is over-sampled and the mean value measured will converge

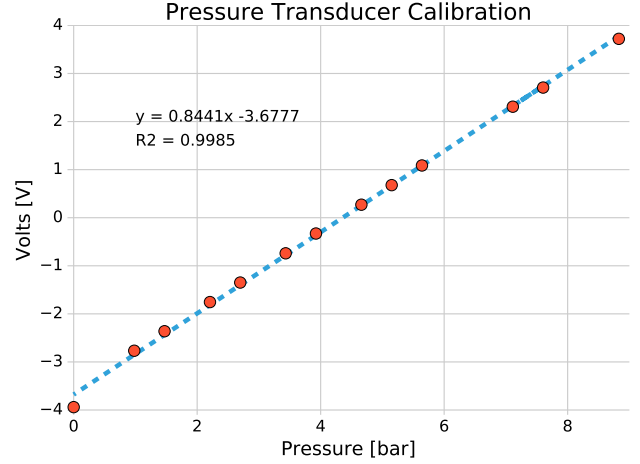


Figure 4: Calibration law for Validyne pressure transducer

faster than in the case where the Nyquist criterion is tightly respected. The acquisition time for each measurement was set at 1 second, hence providing enough samples for a converged mean output.

The balance produces a voltage for each force applied, ideally each voltage is proportional to only one of the three forces. Due to interference between the forces a calibration matrix had to be determined. Furthermore a small offset due to the amplifiers is observed. This yields to the following linear system.

$$\begin{bmatrix} U_x \\ U_y \\ U_m \end{bmatrix} = \begin{bmatrix} A_{xx} & A_{xy} & A_{xm} \\ A_{yx} & A_{yy} & A_{ym} \\ A_{mx} & A_{my} & A_{mm} \end{bmatrix} \begin{bmatrix} F_x \\ F_y \\ M \end{bmatrix} + \begin{bmatrix} B_x \\ B_y \\ B_m \end{bmatrix} \quad (7)$$

By applying consecutively a pure axial force (F_x), side force (F_y) and pitching moment (M), the individual coefficients of eq. (7) can be determined. For example, if a pure axial force is applied the system becomes the following

$$\begin{bmatrix} U_x \\ U_y \\ U_m \end{bmatrix} = \begin{bmatrix} A_{xx} & \cancel{A_{xy}} & \cancel{A_{xm}} \\ A_{yx} & \cancel{A_{yy}} & \cancel{A_{ym}} \\ A_{mx} & \cancel{A_{my}} & \cancel{A_{mm}} \end{bmatrix} \begin{bmatrix} F_x \\ 0 \\ 0 \end{bmatrix} + \begin{bmatrix} B_x \\ B_y \\ B_m \end{bmatrix} \quad (8)$$

and the coefficients can be easily found by applying a linear regression. The balance is mounted on a table which was leveled using a plumb rule. The balance is excited consecutively by a pure axial force, side force and moment. For each force direction 22 different loads are applied to the supports, 11 weights in negative direction and 11 in the positive direction. It must be noted that for the axial component only negative forces can be applied in this setup. The

result of the calibration procedure is given in figures fig. 5, fig. 6 and fig. 7. The coefficients of the linear system can be retrieved from a linear regression. The coefficient of the offset vector are not constant as one would expect. The average value is therefore chosen for the force calculation. After inversion of eq. (8) the force can be found from the following system:

$$\begin{bmatrix} F_x \\ F_y \\ M \end{bmatrix} = \begin{bmatrix} 10.3135 & -1.2211 & -0.0760 \\ 0.0686 & -7.3511 & -0.1465 \\ 0.0034 & -0.0053 & -0.1347 \end{bmatrix} \begin{bmatrix} U_x \\ U_y \\ U_m \end{bmatrix} + \begin{bmatrix} -0.0658 \\ 0.0325 \\ -0.0313 \end{bmatrix} \quad (9)$$

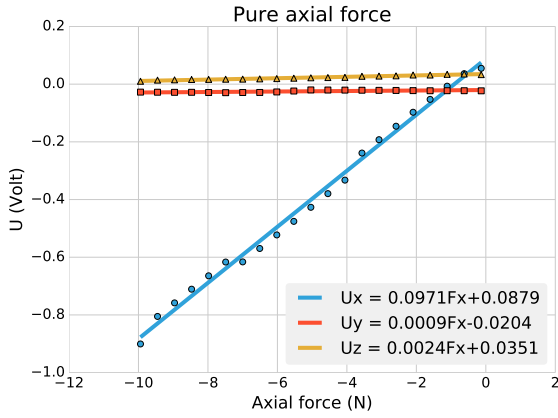


Figure 5: Calibration of the sting balance: Axial force

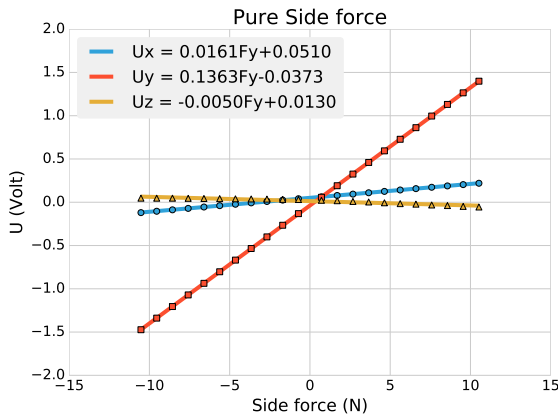


Figure 6: Calibration of the sting balance: Side force

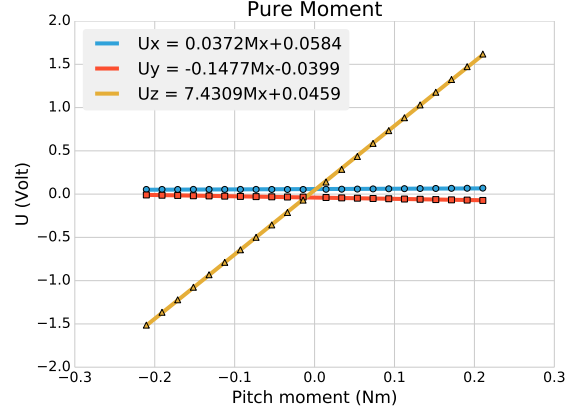


Figure 7: Calibration of the sting balance: Moment

The method to calculate the uncertainty on the balance calibration is discussed in section 5.3. The resulting values are given in the table below.

Measured Variable		Dependent Variable	
δU_x	± 0.0103 V	δF_x	± 0.1059 N
δU_y	± 0.0008 V	δF_y	± 0.0056 N
δU_m	± 0.0029 V	δM	± 0.0004 Nm

Table 1: Uncertainty on the balance calibration.

The uncertainty on the axial force is the largest, this is logical when comparing the linear regressions in fig. 5, fig. 6, fig. 7. The largest variation is found when applying a pure axial force. To evaluate the calibration matrix a validation test is performed in section 4.3.1.

4.3.1. Validation of the calibration matrix

The calibration matrix is validated by comparing the applied force with the measured force. The results are given in fig. 8, fig. 9, fig. 10. The largest relative error is found near the origin. A non-zero error in the origin is due to the variable offset found during the calibration procedure, which has a larger impact on smaller values.

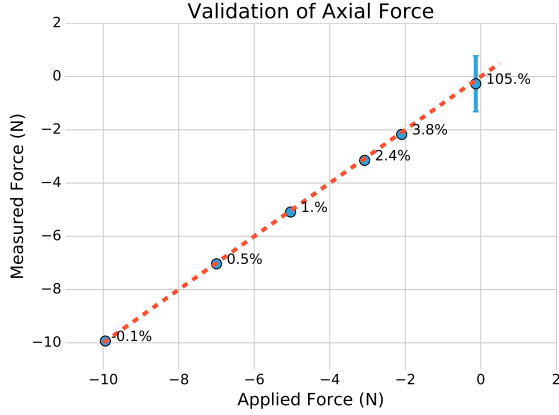


Figure 8: Validation of the sting balance: Axial force

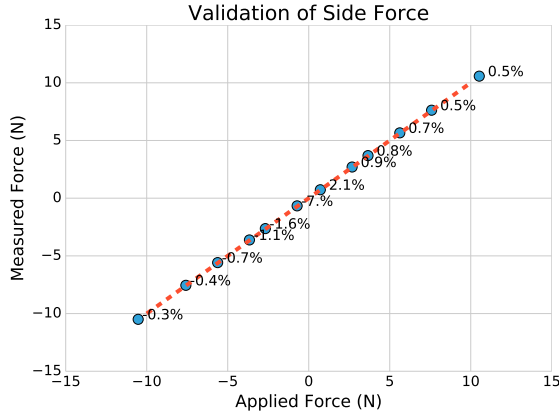


Figure 9: Validation of the sting balance: Side force

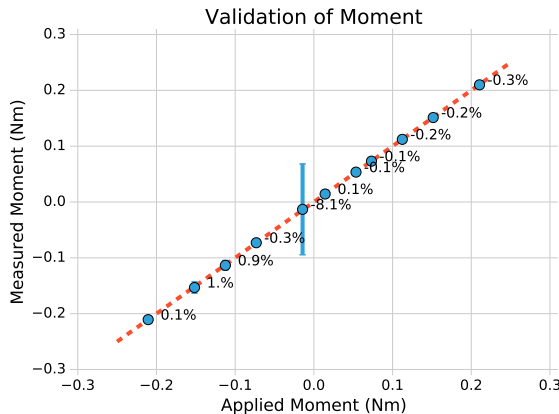


Figure 10: Validation of the sting balance: Moment

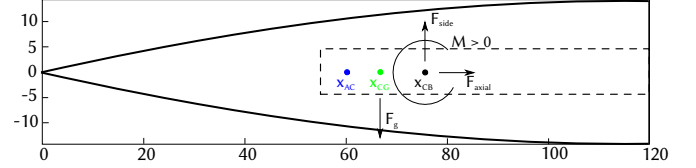


Figure 11: Center of gravity and aerodynamic center of the ogive.

5. Results

5.1. Center of gravity and aerodynamic center

The center of gravity of the balance is derived from measurements without the flow, thus the only force acting on the ogive is its weight (and a small contribution of the balance itself). First of all the total mass acting on the balance can be retrieved from the imaginary lift force.

$$m = \frac{-F_y \cos \alpha + F_x \sin \alpha}{g} = 0.155 \text{ [kg]} \quad (10)$$

Knowing the center of the balance ($X_{CB} = 76\text{mm}$ from the tip of the ogive) the center of gravity of the ogive (X_{CG}) can be computed by the following relation

$$\mathcal{M} = (X_{CB} - X_{CG})F_y \quad (11)$$

$$(X_{CB} - X_{CG}) = \frac{\mathcal{M}}{F_y} = c^{te} \quad (12)$$

Since \mathcal{M} and F_y are vectors, the center of gravity is taken as the mean of the result.

$$(X_{CB} - X_{CG}) = 8.82 \text{ [mm]}$$

The aerodynamic center can be found in the same way, only now the ogive is subjected to the flow. Since the moment in the aerodynamic center is independent from the angle of attack, the aerodynamic center is retrieved from:

$$\mathcal{M}_{AC} = -F_y(X_{CB} - X_{AC}) + \mathcal{M} \quad (13)$$

$$\frac{d\mathcal{M}_{AC}}{dF_y} = 0 \Rightarrow (X_{CB} - X_{AC}) = -\frac{d\mathcal{M}_{CB}}{dF_y} = 15.3 \text{ [mm]} \quad (14)$$

5.2. Aerodynamic coefficients

The ogive has been tested in the wind tunnel at Mach 3.5 at angles of attack from -6° to 6° in order to retrieve forces and aerodynamic coefficients.

Conditions in the test chamber are found by relating the total pressure in the reservoir to the static pressure inside the test section via the isentropic relations for a nozzle. From the Valydine calibration curve (fig. 4), the pressure in the reservoir is found to be $P_0 = 7.70$ bar. Such a pressure is smaller than the value expected a priori and this might be attributed to the process of Valydine calibration (see the calibration section for a description of the faults into the system) or to different working conditions of the compressed air supply line.

The static pressure in the test section is obtained by:

$$P = P_0 \left(1 + \frac{\gamma-1}{2} M^2 \right)^{\gamma/(1-\gamma)} = 0.101 \pm 0.072 \text{ bar } (20 : 1) \quad (15)$$

The static pressure allows a direct computation of the dynamic pressure q_∞ :

$$q_\infty = \frac{\rho U^2}{2} = \frac{\gamma P M^2}{2} = 8.6539 \times 10^4 \pm 809.47 \text{ Pa } (20 : 1) \quad (16)$$

Although the balance is designed to compensate the thermal effects, temperature gradients among strain gauges may alter the results. The first step in processing experimental data is thus compensating this spurious temperature effect. Data was acquired before and after the test, in order to obtain values at zero load. The temperature drift was thus identified and removed by assuming a *linear* growth of the drift in time.

Another interference to the measurements is due to the weight of the ogive and the balance itself. According to the convention, for positive angles of attack, the weight induces an additional axial force, while the normal force and the moment are *reduced*, so that corrected axial force (\mathcal{A}), normal (\mathcal{N}) and momentum (\mathcal{M}) read:

$$\begin{cases} \mathcal{A} = \mathcal{A}_m - mg \sin \alpha \\ \mathcal{N} = \mathcal{N}_m + mg \cos \alpha \\ \mathcal{M} = \mathcal{M}_m + mgd \cos \alpha \end{cases} \quad (17)$$

where measured quantities are identified by the subscript m , while aerodynamic forces are expressed without subscript and are expressed in the center of the balance and d is the distance between center of balance and aerodynamic center. Should be noticed that the forces are currently expressed in the center of balance.

The moment has then to be transported from the center of balance (CB) to the aerodynamic center (AC). Following the convention, we have:

$$\mathcal{M}_{AC} = \mathcal{M}_{CB} + \mathcal{N}(x_{CB} - x_{AC}) \quad (18)$$

Finally, forces are rotated into wind axis, in order to obtain lift and drag, according to:

$$\begin{cases} \mathcal{L} = \mathcal{N} \cos \alpha - \mathcal{A} \sin \alpha \\ \mathcal{D} = \mathcal{N} \sin \alpha + \mathcal{A} \cos \alpha \\ \mathcal{M} = \mathcal{M}_{AC} \end{cases} \quad (19)$$

Notice that according to the definition of aerodynamic center, the moment becomes constant. The aerodynamic forces obtained are shown in fig. 12, fig. 13 and fig. 14, where the uncertainty on the angle has been omitted from the graphics, being approximately equal to 0.2° and thus small with respect to the effect of the other sources of uncertainties. The uncertainties for the aerodynamic forces are obtained by adding the uncertainty due to the calibration curve to the that of the fluctuations of the voltage during the measurement:

$$\delta F = \sqrt{(\delta F)_{\text{calib}}^2 + (\delta F)_{\text{fluct}}^2} \quad (20)$$

Lift and drag coefficients are compared with values obtained with the slender body theory, extended to inclined bodies of revolution. Results are shown in fig. 15, fig. 16 and fig. 17. A comparison with the moment coefficient of the slender body theory is not reported since its formulation requires more insight *with respect to (wrt)* the lift and drag ones. A formulation can be found in [4]. Aerodynamic coefficients are also compared with values obtained with Missile DATCOM, that is found to approach very well the slender body theory prediction for the drag and the measured values for lift and moment coefficients. Should be recalled that the aerodynamic moment computed in the aerodynamic center for a symmetric body is zero: the slightly different values predicted by Missile DATCOM and the measured ones are indeed very small. Uncertainties justifying this behavior may come from imperfections in the ogive, misalignment in the test section and errors in the incidence-mechanism calibration, together with errors in the computation of the exact position of the aerodynamic center.

According to the manual [5], Missile DATCOM employs the Van Dyke hybrid theory for the inviscid component of the forces [6], with viscous corrections by Jorgensen [7].

When comparing the measurements with the slender body theory, one should recall that this theory is valid for *inviscid* flows around *very* slender bodies of revolution. It's well known that the parasitic drag is usually not well predicted by this theory, as well as the lift coefficient, that is usually slightly different than the theoretical value $C_L = 2\alpha$.

The uncertainty of the coefficients is reported in terms of error bars and is expressed for a 95% confidence level. As can be seen from

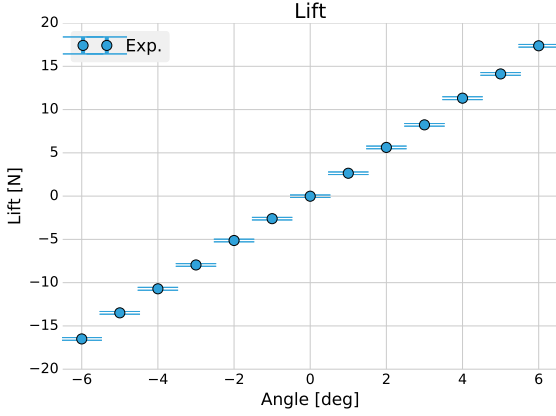


Figure 12: Lift

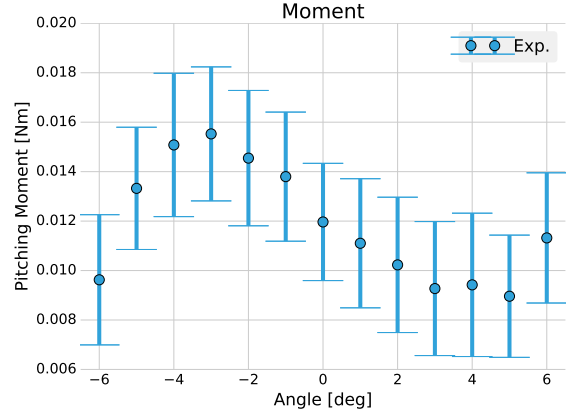


Figure 14: Aerodynamic moment

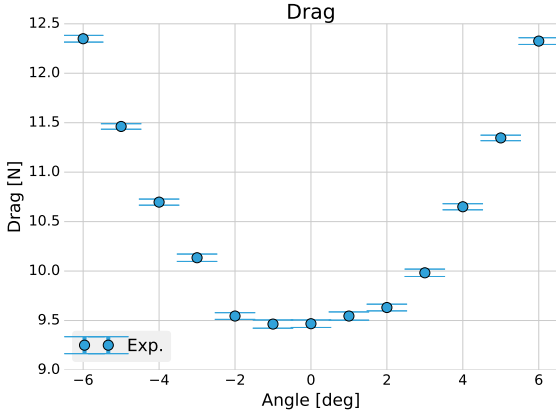


Figure 13: Drag

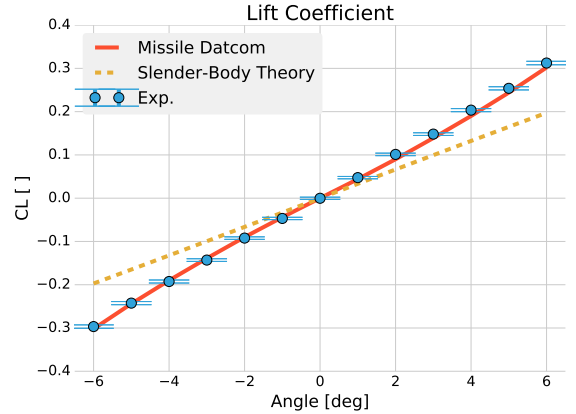


Figure 15: Lift coefficient

the formula previously reported, the uncertainty on the aerodynamic coefficients depends on *all* the three measured quantities: pressure, angle and forces.

5.3. Uncertainty analysis

The method for uncertainty quantification is explained with a practical example. Due to the number of measured values (sc. 5) and the use of a linear fit (and the resulting linear system) the number of parameters which carry uncertainty is very large. To keep the uncertainty quantification simple and understandable a couple of simplification and linearizations are applied which will be explained in the remainder of this section.

The method is explained for the calculation of the lift coefficient

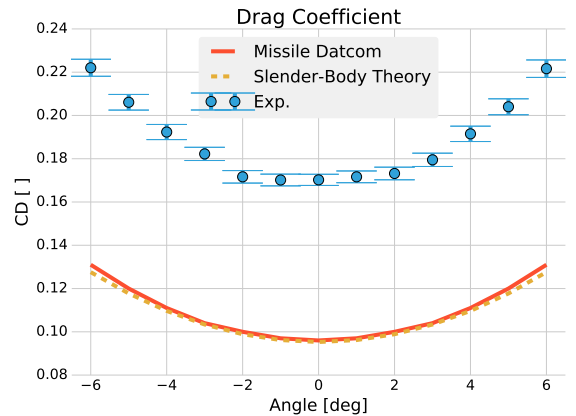


Figure 16: Drag coefficient

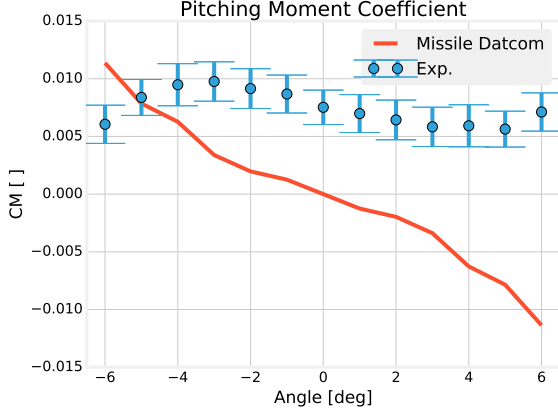


Figure 17: Moment coefficient

(C_L) given in eq. (21). The lift force can be expressed in terms of axial and side force and when writing the angle of attack in radians the linearization in eq. (22) can be used for small angles. The dynamic pressure can be written in terms of the Mach number and the stagnation pressure measured by the Valydine.

$$C_L = \frac{L}{\frac{1}{2}\rho V^2 S_{ref}} \quad (21)$$

$$L = F_y \cos \alpha - F_x \sin \alpha \cong F_y - F_x \alpha \quad (22)$$

This results in eq. (23). It is now assumed that the values for M , γ and S_{ref} are absolute and constant during the experiments.

$$C_L = \frac{F_y - F_x \alpha}{\frac{\gamma}{2} M^2 p S_{ref}} \quad (23)$$

The general form for the uncertainty on C_L is then given by

$$\begin{aligned} \delta C_L^2 = & (\delta F_y)^2 \left(\frac{1}{\frac{\gamma}{2} M^2 p S_{ref}} \right)^2 + (\delta F_x)^2 \left(\frac{\alpha}{\frac{\gamma}{2} M^2 p S_{ref}} \right)^2 \\ & + (\delta \alpha)^2 \left(\frac{F_x}{\frac{\gamma}{2} M^2 p S_{ref}} \right)^2 + (\delta p)^2 \left(\frac{F_y - F_x \alpha}{\frac{\gamma}{2} M^2 p^2 S_{ref}} \right)^2 \end{aligned} \quad (24)$$

The value now needed to be defined is the uncertainty on the measured variables. All the variables in eq. (24) are indirectly measured and are retrieved from a linear regression. The following example for the balance output is thus also valid for the pressure and incidence measurement. The variance of a sampled mean can

be estimated by

$$s_U^2 = \frac{1}{N-1} \sum_{i=1}^N (U_i - \bar{U})^2 \quad (25)$$

with N the number of samples and \bar{U} the sampled mean (output voltage). The quantity $(U_i - \bar{U})$ is now defined as the local error e_i , which is the difference between the measured voltage and the linear fit, as illustrated in fig. 18.

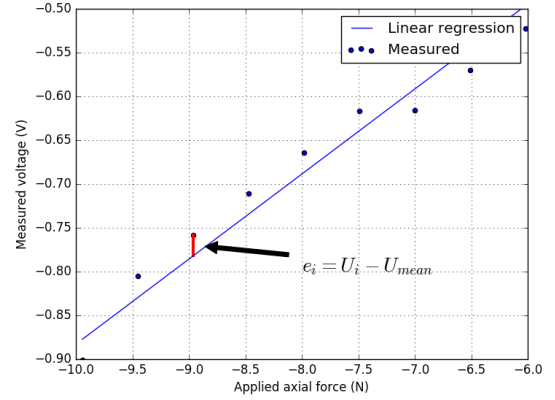


Figure 18: Definition of the error on the linear regression.

The confidence interval on the measured voltage can then be computed, assuming a student distribution, by

$$\delta U = \pm \frac{s_U t_{N-1, 1-\alpha/2}}{\sqrt{N}} \quad (26)$$

with $(1 - \alpha)$ the desired confidence interval. The final expression on the uncertainty of the measured voltage can thus be written as:

$$U = U_{measured} \pm \delta U \text{ volts } 100 : \alpha \text{ odds} \quad (27)$$

For the uncertainty of the dependent variable, in this case the force on the balance, only the mayor contributor is considered (i.e. neglecting the interference factors and their own uncertainties). Which results in

$$\delta F_i = A_{ii} \delta U_i \quad (28)$$

with i the force direction or moment on the balance. For every measured variable the uncertainty on the dependent variable is summarized in table 2.

Measured variable		Dependent variable	
δU_x	± 0.0103 V	δF_x	± 0.1059 N
δU_y	± 0.0008 V	δF_y	± 0.0056 N
δU_m	± 0.0029 V	δM	± 0.0004 Nm
δU_p	± 0.0850 V	δP	± 0.0718 bar
δN_t	± 7	$\delta \alpha$	$\pm 0.2^\circ$

Table 2: Uncertainty on the measured variables and their dependent variable for a confidence interval of 95%.

Mass of TiO_2 [g]	Mass of Oil [g]	Comments
1	6	Too liquid
6	6	Too liquid
9	6	Ok

Table 3: Compound mixture attempts

6. Flow Visualization

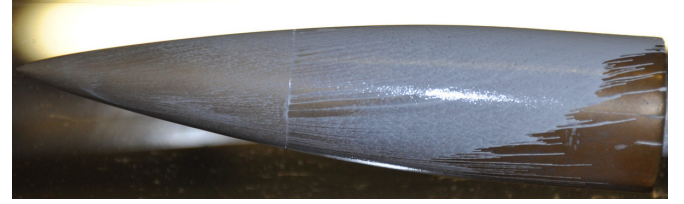
6.1. Oil visualization

Oil visualization is a technique very useful to understand complex flow patterns around objects. It's based on the experimental evidence that a fluid compound with right viscosity and density properties, as for example a mixture of oil and titanium dioxide TiO_2 , can be entrained by the flow shear stress and behave like the stress-lines over the surface of the body. In the frame of the experiment the compound chosen to visualize the flow was olive oil with addition of titanium dioxide to achieve the desired viscosity of the oil layer in order to be able to detect the shear lines and, hence, deduct the flow pattern near the ogive surface.

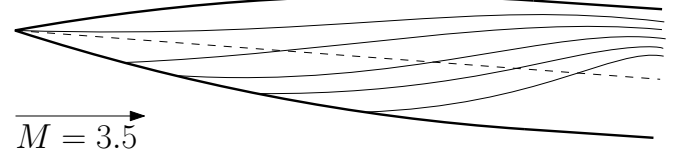
Before running the wind tunnel several attempts have been made to converge to the most effective ratio between the oil and the TiO_2 powder that are qualitatively summarized in table 3.

The visualization tests have been performed for a value of the Angle of Attack (AoA) = 5° and the best results are reported in fig. 19 and fig. 20.

As it is possible to see, all the streamlines originating from the apex of the nosecone are converging in the top-rear part of the ogive. In [8] is reported that the flow around an ogive-cylinder revolution body at $M = 2$ is characterized by shear-lines joining along a separation line S_1 that begins at the station $\frac{x}{L} = 4$. This result is in accordance with ours since for higher Mach numbers the separation is expected to happen further downstream *wrt* lower ones



(a) Oil-Visualization of the ogive at $\alpha = 5^\circ$



(b) Shear-lines interpretation sketch

Figure 19: Comparison of the visualization with an interpretation sketch

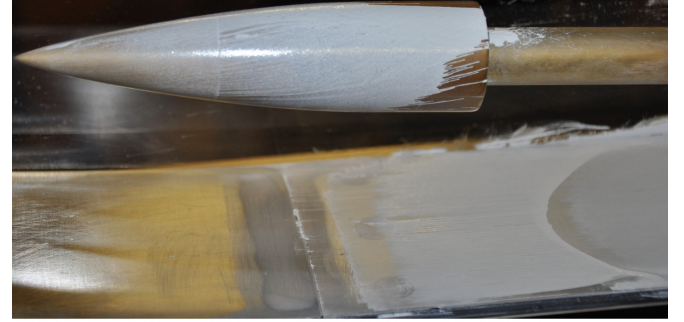


Figure 20: Oil-Visualization with shock footprint

[9, p. 16] and in the case examined in this work no evidence of separation is encountered.

In fig. 20, is clearly noticeable an hyperbolic shape on the lower wall of the wind tunnel. This hyperbolic shape of the footprint identifies the nature of the shock occurring at the nose tip of the ogive as a conical shock. In facts, regarding the fig. 21, the intersection of a cone with a plane is nonetheless an hyperbola.

6.2. Shadowgraph and Schlieren

Shadowgraph and Schlieren are two techniques that translate density differences into amplitude differences that our eyes can detect. The basic working principle of those techniques is based on the experimental evidence that light traversing a medium is slowed down *wrt* its velocity in vacuum 3×10^8 [m/s]. This velocity decrease is represented by the refractive index $n = \frac{c}{c_0}$. For gases there exist a linear relationship between density and refractive index as

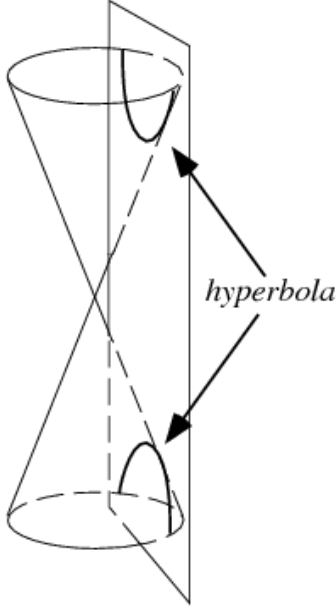


Figure 21: Intersection of a cone with a plane

shown in eq. (29).

Schlieren and shadowgraph are somehow related, differences can be however reported: schlieren illumination responds to the first derivative of refractive index, and hence of density, while for shadowgraph the relation is related to the second derivative of it.

$$n = 1 + k\rho \quad (29)$$

k is the Gladstone-Dale factor and has a weak dependence on temperature, wave-length (λ), gas nature. As reported in [10], optical inhomogeneities refract or bend the light rays proportionally to refractive index gradients over the cross-section plane normal to the direction of the rays. The ray curvatures are given by:

$$\frac{\partial^2 x}{\partial z^2} = \frac{1}{n} \frac{\partial n}{\partial x} \quad (30)$$

$$\frac{\partial^2 y}{\partial z^2} = \frac{1}{n} \frac{\partial n}{\partial y} \quad (31)$$

the equations can be further integrated to get the component of the angular deflection of the rays:

$$\epsilon_x = \frac{L}{n} \frac{\partial n}{\partial x} \quad (32)$$

$$\epsilon_y = \frac{L}{n} \frac{\partial n}{\partial y} \quad (33)$$

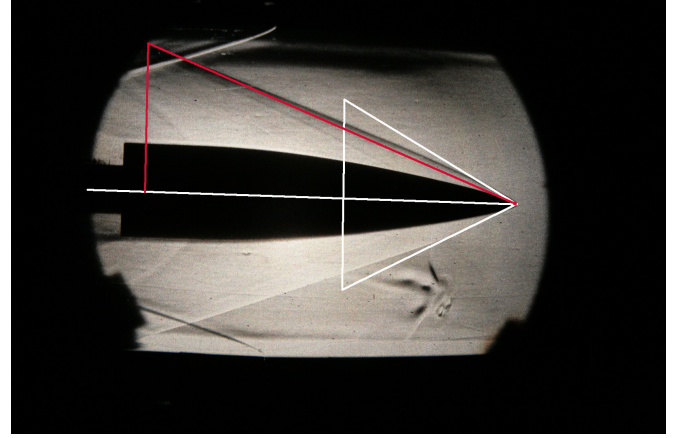


Figure 22: Schlieren Image of the ogive at $\alpha = 0^\circ$

From those equations we can infer that light beams are bended towards zones with higher refractive index, and taking into account eq. (29), hence, towards zones with higher density. In fig. 26 is showed a schlieren image of the nosecone taken into account in this analysis. At the nose tip is clearly visible a strong change in illumination, that is hence related to a strong gradient of density, due to a shockwave, that has a typical conical shape. The conical shape of the shockwave can be also inferred by the hyperbolic footprint that can be noted on the back of the ogive: it could be related, as in the case of the oil flow visualization, to the intersection of the conical shock with the side walls of the wind tunnel.

To compute the angle of the shockwave wrt the flow direction, the FOSS program GIMP has been used. The length of the lines as, for example, showed in fig. 22, has been computed and from them the angle between the shockwave and the flow direction has been calculated.

Comparing the two pictures for the axial-flow schlieren (fig. 22) and for the inclined-flow (fig. 25) can be noted how in the first figure the upper part of the shock is black while the bottom part is white, in the second figure both sides are black. This indicates that the knife configurations are different: horizontal knife for fig. 22 and vertical for fig. 25.

6.2.1. Axial Flow

With reference to fig. 22, that shows the ogive in pure axial non-inclined flow, it is possible to note how the shockwave is not a straight line but it has a curved slope. This curved shape is addressable to the fact that the flow, once deflected by the front shockwave, generates expansion fans continuously along the ogive

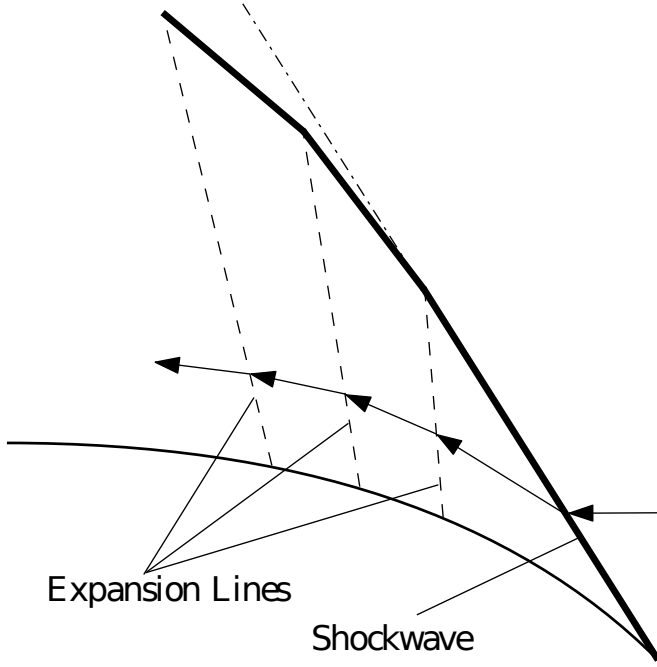


Figure 23: Deflected flow expands to follow the surface slope

surface since it has to realign with the surface slope. This expansions also deflect the shockwave angle downstream generating a curved shock as schematized in fig. 23.

From this evidence a issue arises about computing the shock angle: it should be computed considering the line tangent at the first part of the wave attached to the nose rather than considering a line that fits the shock wave for all its length. For the case of pure axial flow the result achieved considering the first strategy lead to best results compared to the second with a calculated angle of 30° instead of 22° , with a theoretical angle given by the graph reported in fig. 1 of $\sim 28^\circ$.

The discrepancy of the computed angle from image processing wrt the angle predicted by the Taylor-Maccoll graph can be addressed to a non-perfect alignment of the camera when taking the schlieren pictures, together with the incertitude for the detection of the values on the graph of fig. 1 that has a resolution of 10° for the cone semiangle and 0.2 for the Mach number.

6.2.2. Inclined Flow

A direct computation of the angles spaced between the shock wave and the ogive axis on the fig. 25, as reported in fig. 26 using lengths in pixels, returns values of $\hat{\sigma}_{\text{top}} = 22^\circ$ and $\hat{\sigma}_{\text{bot}} = 29^\circ$ degrees re-

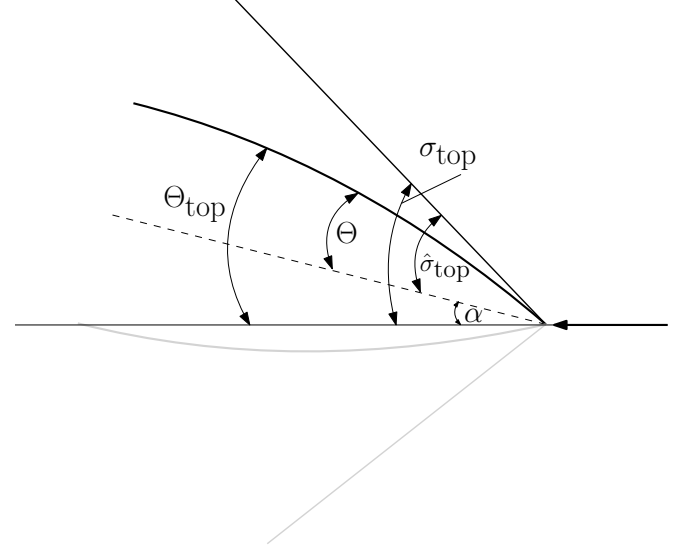


Figure 24: Schematic of the angles for inclined configuration

Angle	Computed Value	Predicted Value (fig. 1)
α		6°
Θ		16°
Θ_{top}		22°
Θ_{bot}		10°
$\hat{\sigma}_{\text{top}}$	22°	-
σ_{top}	28°	30°
$\hat{\sigma}_{\text{bot}}$	29°	-
σ_{bot}	22°	20°

Table 4: Summary of computed angles in the schlieren

spectively for the top and bottom shocks. As sketched in fig. 24, the real angles to be used with the Taylor-Maccoll graph are obtained as in eq. (34). The assumption made here is expected to be valid only in 2D, while an extension to 3D is not formally rigorous. The results obtained can nonetheless provide a feeling of the physical phenomenon. The results are summarized in table 4.

$$\begin{aligned}
 \Theta_{\text{top}} &= \Theta + \alpha \\
 \sigma_{\text{top}} &= \hat{\sigma}_{\text{top}} + \alpha \\
 \Theta_{\text{bot}} &= \Theta - \alpha \\
 \sigma_{\text{bot}} &= \hat{\sigma}_{\text{bot}} - \alpha
 \end{aligned} \tag{34}$$

²the image is upside-down due to the optical setup

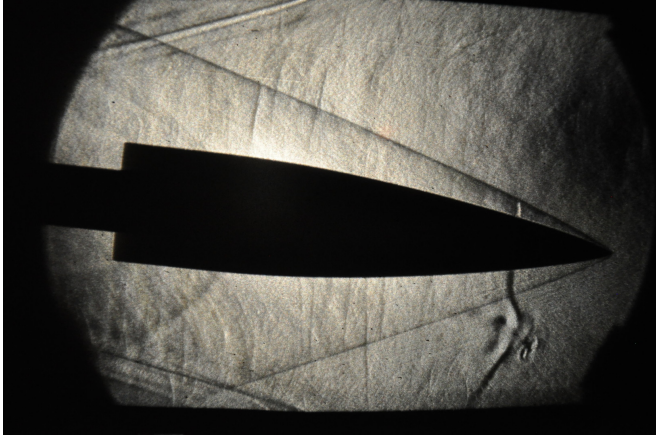


Figure 25: Schlieren Image of the ogive at $\alpha = 5^{\circ}$

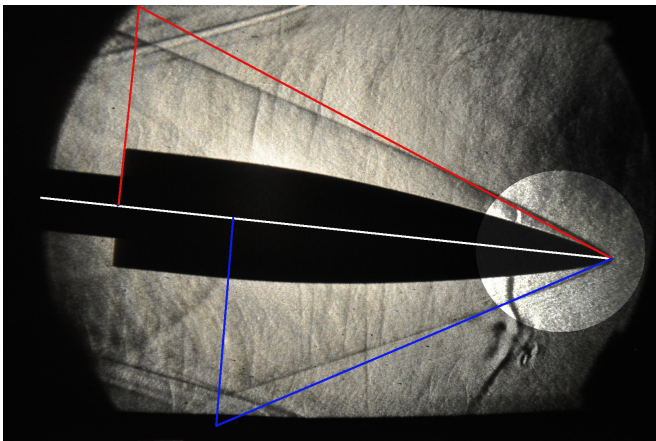


Figure 26: Schlieren Image of the ogive at $\alpha = 5^{\circ}$

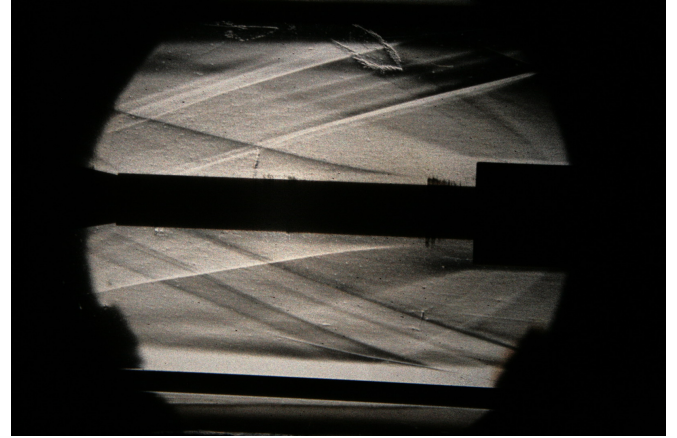


Figure 27: Rear recompression of the flow

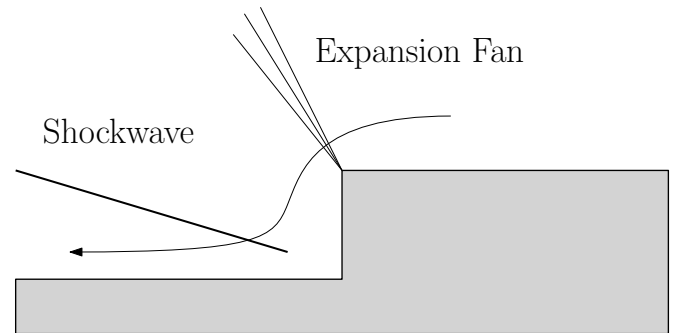


Figure 28: Schematic of the rear recompression of the flow

6.2.3. Rear-part of the ogive

In fig. 27 is possible to see the shock pattern of the rear part of the ogive. It's possible to note another set of two shocks just after the end of the aftbody of the nosecone. Those shocks are caused by the flow that is turning around the vertical rear-wall of the ogive that has to realign with the main flow direction causing a compression and, hence, shocks. The situation is schematized in fig. 28.

6.3. Water Table

As reported in [11], an analogy between the frictionless motion of shallow water and the isentropic flow of a compressible gas can be derived for water flowing in a rectangular duct, in this case the analogue gas should have a specific heat ratio $\gamma = 2$, or in a duct whose dimension are related by eq. (35) (being z, y the physical

dimension of the cross-section)³.

$$z = Cy^n \quad (35)$$

For the particular case of rectangular cross-section duct (for the hydraulic part), the direct comparison of the continuity equation of the free-surface water flow and isentropic gas (eq. (36)) leads to assume that the water depth ζ is analogue to the density ρ .

$$\begin{aligned} \frac{\partial \zeta u}{\partial x} + \frac{\partial \zeta v}{\partial y} &= 0 \\ \frac{\partial \rho u}{\partial x} + \frac{\partial \rho v}{\partial y} &= 0 \end{aligned} \quad (36)$$

Moreover if the energy equation for both flows is considered (eq. (37)), the water depth is also analogue to the isentropic gas temperature T .

$$\begin{aligned} \zeta + \frac{V^2}{2g} &= \zeta_0 \\ T + \frac{V^2}{2C_p} &= T_0 \end{aligned} \quad (37)$$

Since in isentropic flow density and temperature are related by eq. (38), the two analogies can hold together only if $\gamma = 2$. The relation between depth and pressure is hence given by eq. (39).

$$\frac{\rho_0}{\rho} = \left(\frac{T_0}{T} \right)^{\frac{1}{\gamma-1}} \quad (38)$$

$$\frac{p}{p_0} = \left(\frac{\zeta}{\zeta_0} \right)^2 \quad (39)$$

6.3.1. Estimation of the water depth

The Mach number in the wind tunnel is provided to be $M = 3.5$. Considering the isentropic relation that returns the total-pressure-to-static-pressure ratio given by eq. (40) and again eq. (39) the right depth ratio is $\frac{\zeta_0}{\zeta} = 8.7334$.

³In facts if a general form of the duct cross section is considered (see eq. (35)), the specific heat ratio does not have to be equal to 2 anymore. The analogue γ can be tuned to be in analogy with real-existing gases (e.g. with a triangular duct $\gamma = 1.5$)

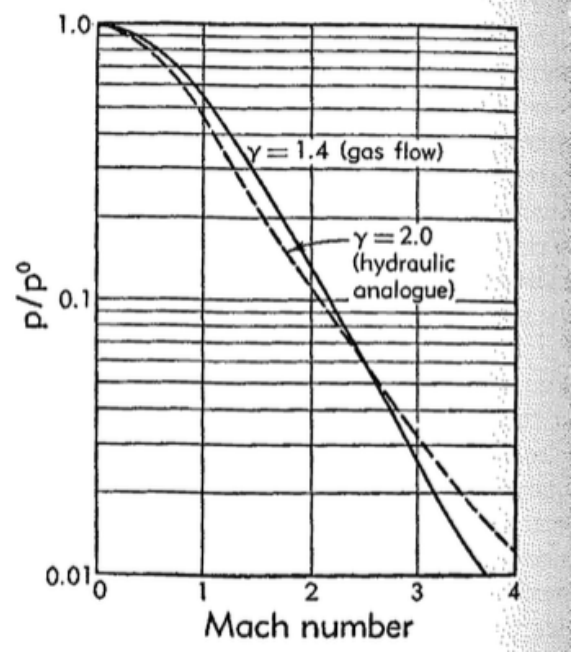


Figure 29: Validity of the water table analogy

$$\frac{p_0}{p} = \left(1 + \frac{\gamma-1}{2} M^2 \right)^{\frac{\gamma}{\gamma-1}} \quad (40)$$

The idea was to keep the shallow water channel with a depth of $\zeta = 5$ [mm], so the depth of the still water reservoir has been set to $\zeta_0 = 45$ [mm].

6.3.2. Validity of the hydraulic analogy

In [12] a figure displaying the validity of the hydraulic analogy in terms of pressure-ratio is provided and is here reported for reference in fig. 29. As it's possible to see in the situation analyzed in this work, quantitatively speaking, the analogy is not strictly valid. The best situation would held for a lower Mach number. The qualitative analysis of the flow topology can, by the way, be however performed even if the effective shock angle will be higher in the water table since, being $\frac{p}{p_0}$ higher, for eq. (40) the Mach number will be lower leading to a higher shock angle.

6.3.3. Qualitative Flow Pattern Analysis

As reported in the previous section, in fig. 30 is possible to note how the shock angle is slightly higher than fig. 22. Nonetheless is



Figure 30: Picture of ogive in the water table

possible to appreciate also the expansion fan at the rear-edges of the ogive and the two rear shock waves discussed in section 6.2.3. The shocks in the water table visualization are showing up as solid thin lines as in the schlieren pictures, but small waves of small wave-length are appearing as a disturbance. These waves are the capillary waves typical of the free-surface shallow water scenario. Moreover the attachment point of shock is not clear since the water is twirling and climbing the body surface.

Acronyms

AoA Angle of Attack

FOSS Free and Open Source Software

GIMP GNU Image Manipulation Program

wrt with respect to

VKI von Karman Institute

NI National Instruments

DAS Data Acquisition System

Nomenclature

α Angle of Attack

$\epsilon_{x,y}$ angular deflection of a light ray

\mathcal{D} drag

\mathcal{L} lift

\mathcal{M} pitching moment

ρ density

σ shockwave angle

Θ cone or ogive semi-angle

θ angular coordinate

ς water depth in the channel

A axial force

c velocity of light

c_0 velocity of light in vacuum

D base caliber of the ogive

F $F = \frac{L}{D}$

g gravity field

h enthalpy

k Gladstone-Dale factor for refraction

L length of the ogive

m mass

N normal force

n refractive index

p pressure

q_∞ free stream dynamic pressure

T temperature

u_r radial component of the velocity

V voltage

References

- [1] A. H. Shapiro, "The dynamics and thermodynamics of compressible fluid flow (vol2)," 1954.
- [2] G. I. Taylor and J. W. Maccoll, "The air pressure on a cone moving at high speeds. i," in *Proceedings of the royal society of london a: Mathematical, physical and engineering sciences*, vol. 139, The Royal Society, 1933, pp. 278–297.
- [3] H. W. Liepmann and A. Roshko, *Elements of gasdynamics*. Courier Corporation, 1957, 468 pp., Google-Books-ID: LvgD47sRQaUC, ISBN: 978-0-486-41963-3.
- [4] H.-S. Tsien, "Supersonic flow over an inclined body of revolution," *Journal of the aeronautical sciences*, vol. 5, no. 12, pp. 480–483, 1938.
- [5] W. B. Blake, "Missile datcom: User's manual-1997 FORTRAN 90 revision.," DTIC Document, 1998.
- [6] Milton D. Van Dyke, "First- and second-order theory of supersonic flow past bodies of revolution," *Journal of the aeronautical sciences*, vol. 18, no. 3, pp. 161–178, Mar. 1951, ISSN: 1936-9956.
- [7] L. H. Jorgensen, "Prediction of static aerodynamic characteristics for space-shuttle-like and other bodies at angles of attack from 0 deg to 180 deg," 1973.
- [8] D. Pagan, P. Molton, and J. Delery, "Basic experiment on a supersonic vortex flow around a missile body," *Journal of spacecraft and rockets*, vol. 29, no. 3, pp. 373–378, May 1992, ISSN: 0022-4650, 1533-6794.
- [9] E. R. Keener, "Oil flow separation patterns on an ogive forebody," *AIAA journal*, vol. 21, no. 4, pp. 550–556, 1983.
- [10] G. S. Settles, *Schlieren and shadowgraph techniques: Visualizing phenomena in transparent media*. Springer Science & Business Media, 2001, 412 pp., Google-Books-ID: HWtB2R0gWFgC, ISBN: 978-3-540-66155-9.
- [11] W. H. Loh, *Modern developments in gas dynamics: Based upon a course on modern developments in fluid mechanics and heat transfer, given at the university of california at los angeles*. Springer Science & Business Media, Dec. 6, 2012, 394 pp., Google-Books-ID: sqzbB-wAAQBAJ, ISBN: 978-1-4615-8624-1.
- [12] A. H. Shapiro, "Free-surface water table," *Physical measurements in gas dynamics and combustion*, High Speed Aerodynamics and Jet Propulsion, vol. 9, pp. 309–321,